Journal of Catalysis 314 (2014) 10–20

Contents lists available at ScienceDirect

Journal of Catalysis

journal homepage: www.elsevier.com/locate/jcat

Verifying the mechanism of the ethene-to-propene conversion on zeolite H-SSZ-13

Weili Dai [a], Xiaoming Sun [a,b], Bo Tang [a], Guangjun Wu [a], Landong Li [a,*], Naijia Guan [a], Michael Hunger [b,*]

[a] Key Laboratory of Advanced Energy Materials Chemistry (Ministry of Education), College of Chemistry, Nankai University, Tianjin 300071, PR China
[b] Institute of Chemical Technology, University of Stuttgart, 70550 Stuttgart, Germany

ARTICLE INFO

Article history:
Received 10 January 2014
Revised 10 March 2014
Accepted 11 March 2014
Available online 19 April 2014

Keywords:
SSZ-13
Ethene-to-propene conversion
Framework dealumination
Brønsted acid sites
Naphthalene-based carbenium ions

ABSTRACT

Several types of microporous molecular sieves with similar n_{Si}/n_{Al} ratios (except for SAPO-34) and different pore structures were prepared and applied as ethene-to-propene (ETP) catalysts. H-SSZ-13 zeolite consisting of chabazite cages connected via 8-ring windows possessed the highest adsorption capacity for ethene and exhibited the best activity in the ETP conversion. The decreasing amount of Brønsted acid sites after dealumination of H-SSZ-13 caused a prolonged lifetime of the catalyst in the ETP reaction. The reaction mechanism and deactivation behavior of H-SSZ-13 catalysts during the ETP process were investigated by in situ FT-IR, UV/Vis, GC–MS, TGA and ^{1}H MAS NMR methods. Ethene was rapidly oligomerized and converted into naphthalene-based carbenium ions, playing a significant role in the ETP reaction. The accumulation of these species lead to the formation of polycyclic aromatics, which are responsible for a total blocking of H-SSZ-13 pores, and cause the deactivation of the catalyst.

1. Introduction

The production of propene has received broad attention in recent years due to the increasing demand for propene derivatives, especially polypropene [1]. To meet the increasing demand for propene, several strategies have been proposed for propene production, e.g. the dehydrogenation of propane [2], the catalytic cracking of C_4 alkenes to propene [3,4], the metathesis of ethene and 2-butene [5,6], and the conversion of methanol/ethanol to propene [7–10]. Recently, the direct conversion of ethene to propene (ETP) without any addition of other hydrocarbons was proposed as a new alternative to produce propene. This would be an interesting reaction for the production of propene, particularly when it is combined with the dehydration of ethanol/bio-ethanol to ethene, a new alternative route to produce propene from renewable feedstock can be opened thereafter.

The ETP reaction was first observed on olefin metathesis catalysts, e.g. supported molybdenum [11] and tungsten catalysts [12]. Recently, Iwamoto et al. [13–16] found that the ETP reaction can be realized over Ni/MCM-41 catalysts prepared via template ion exchange method, but with lower ethene conversion (68%) and propene selectivity (48%). More recently, Perea et al. [17] disclosed that the ethene conversion can be improved to about 80% over Ni/AlMCM-41 with few acid sites, but the selectivity was nearly not changed. Similar to Ni/AlMCM-41, also Ni/AlMCM-48 [18] was proved to be a good catalyst in the ETP reaction. Basset and co-workers [19] found that the ETP reaction with high selectivity to propene (95%) can be obtained over tungsten hydride supported on γ-alumina, i.e. $W(H)_3/\gamma\text{-}Al_2O_3$, but the ethene conversion starting with 40% drop to 10% after a time-on-stream (TOS) of 20 h. In addition, several kinds of microporous molecular sieves have been studied as possible ETP catalysts [20–24], and the acidity and the pore structure of molecular sieves were proposed to be key factors controlling the ETP reaction. SAPO-34, with chabazite cages connected via 8-ring windows exhibits high selectivity to propene in the ETP reaction, but the aluminosilicate analogue H-SSZ-13 with stronger acidity was scarcely studied in the ETP conversion. The relationship between acidity, ethene absorption ability, and ETP activity of microporous molecular sieves is not clear until now and, therefore, is the goal of the present work. In addition, the reaction mechanism of the ETP conversion has been intensively studied in the past years, and a route was accepted consisting of an ethene dimerization to form butene, which is involved in a metathesis reaction with another ethene molecules leading to propene [20,23,25–27]. However, to the best of our knowledge, the reaction mechanism in the steady state of the ETP reaction and the deactivation behavior of the catalysts,

* Corresponding authors. Fax: +86 22 2350 0341 (L. Li). Fax: +49 711 685 64081 (M. Hunger).
E-mail addresses: lild@nankai.edu.cn (L. Li), michael.hunger@itc.uni-stuttgart.de (M. Hunger).

http://dx.doi.org/10.1016/j.jcat.2014.03.006
0021-9517/

especially detailed spectroscopic investigations of the above-mentioned route of the ETP reaction, are missing until now and are, therefore, also aims of this work.

In this study, several types of microporous molecular sieves with similar n_{Si}/n_{Al} ratios and different pore structures were prepared and applied as ETP catalysts. The ethene adsorption abilities of these catalysts were studied via dynamic breakthrough measurements, and the ETP catalytic performances of the samples were evaluated in a fixed-bed reactor. The effects of acid densities on the catalytic performance were investigated by dealumination and focused on H-SSZ-13, which exhibits the highest activity in the ETP conversion. The organic intermediates formed on H-SSZ-13 catalysts during the different states of the ETP reaction were analyzed by in situ FTIR, ex situ UV/Vis, TGA, and GC–MS methods. Specifically, the dynamic changes in the Brønsted acid sites and carbenium ions during the ETP reaction are monitored by ^{1}H solid-state NMR spectroscopy using ammonia-loaded catalyst samples. Based on the catalytic and spectroscopic results, the reaction mechanism and the deactivation behavior of H-SSZ-13 catalysts in the ETP reaction are discussed.

2. Experimental section

2.1. Preparation of the materials

A series of aluminosilicate zeolites in their Na-form with different framework structures (MOR: Na-modenite, BEA: Na-Beta, MFI: Na-ZSM-5, EUO: Na-EU-1, CHA: Na-SSZ-13) were provided by Sinopec, China. Then, the calcined Na-type aluminosilicate samples were converted to their proton forms by refluxing three times in 0.1 M NH_4NO_3 solutions for 6 h, followed by drying at 343 K for 12 h and calcination at 873 K for 4 h. The SAPO-34 sample was synthesized by a hydrothermal method using TEAOH (tetraethylammonium) as structure-directing agents, and the batch composition was 1 Al_2O_3:1 P_2O_5:0.6 SiO_2:0.5 TEAOH:77 H_2O [28,29]. Then, the as-synthesized SAPO-34 was calcined in flowing synthetic air at 873 K for 4 h, and the parent H-SSZ-13 samples were dealuminated by treatment in 13.0 M HNO_3 solution at 373 K for 20, 40, and 60 h (20 mL g^{-1} zeolite), and named as deAl-SSZ-13(20), deAl-SSZ-13(40), and deAl-SSZ-13(60), respectively.

2.2. Characterization of the materials

X-ray diffraction (XRD) patterns of the calcined samples were recorded on a Bruker D8 diffractometer with Cu Kα radiation (λ = 1.5418 Å) at 5–50° and with a scan rate of 2θ = 6.0°/min.

The chemical compositions of the samples were determined by inductively coupled plasma emission spectrometry (ICP-AES) on a Thermo IRIS Intrepid II XSP atomic emission spectrometer.

The surface areas and nitrogen adsorption isotherms of the calcined samples were measured by means of nitrogen adsorption at 77 K on a Quantachrome iQ-MP gas adsorption analyzer. Before the nitrogen adsorption, samples were dehydrated at 473 K for 2 h. The total surface area was calculated via the Brunauer Emmett Teller (BET) equation and the microporous pore volume was determined using the *t*-plot method.

The solid-state NMR investigations of the catalyst framework were performed with hydrated samples on a Bruker Avance III 400WB spectrometer at the resonance frequency of 104.3 MHz for ^{27}Al nuclei. The MAS spectra were recorded upon $\pi/6$ single pulse excitation, with the repetition time of 0.5 s, and the sample spinning rate of 8 kHz. To avoid hydrolyses of framework bonds, the hydration of the samples was performed not longer than one day before the NMR characterization by exposing them to an atmosphere saturated with the vapor of an aqueous $Ca(NO_3)_2$ solution at ambient temperature.

Deuterated acetonitrile (CD_3CN) was used as probe molecule to measure the acid strength of the catalysts. The measurements were performed with dehydrated samples by means of ^{1}H MAS NMR spectroscopy utilizing a Bruker Avance III 400WB spectrometer at the resonance frequency of 400.1 MHz, with $\pi/2$ single pulse excitation, the repetition time of 10 s, and the sample spinning rate of 8.0 kHz using a 4.0 mm MAS NMR probe. Before the ^{1}H MAS NMR studies of the catalysts, these materials were dehydrated at 673 K in vacuum (pressure below 10^{-2} Pa) for 10 h. Then, the dehydrated samples were loaded with 70 mbar acetonitrile-d_3 (99.9% deuterated) and, subsequently, evacuated at 298 K for 1 h to eliminate physisorbed acetonitrile.

The experimental setup used for dynamic breakthrough measurements is shown in Scheme S1. The downstream gas mixture was monitored using an Omni Star TM mass spectrometer. In a typical experiment, 0.2 g of the catalyst was treated at 673 K under flowing He gas (20 mL/min) for 2 h. After the temperature was decreased to room temperature, the gas flow was switched to an ethene/helium mixture (ethene: 250 ppm) at the same total flow rate. The complete breakthrough of ethene was indicated by reaching a downstream gas composition equal to that of the feed gas. A reference breakthrough experiment was recorded at the same conditions without catalysts.

2.3. Catalytic studies of the zeolites under study

The ETP reaction was investigated in a fixed-bed reactor at atmospheric pressure. Typically, 0.2 g of the catalyst (sieve fraction, 0.25–0.5 mm) was placed in a stainless-steel reactor (5 mm i.d.) and activated under flowing helium gas at 673 K for 1 h. After the temperature was decreased to the desired reaction temperature, the reactant, i.e., C_2H_4, diluted with high purity helium was introduced to start the reaction. The total flow rate (F) was 20 mL/min, and the partial pressure of C_2H_4, denoted as $p(C_2H_4)$, was 50.0 kPa. The products were analyzed by an on-line chromatograph HP5890/II with flame ionization detector (FID) and a packed-column Porapak Q to separate the hydrocarbons.

2.4. Characterization of entrapped organic compounds on the used catalysts

The nature of the organic compounds formed on the catalyst during the ETP reaction was in situ monitored by Fourier transform infrared (FTIR) spectroscopy. FTIR spectra were recorded in the diffuse reflection mode on a Bruker Tensor 27 spectrometer, equipped with a high sensitivity MCT detector cooled by liquid nitrogen and an in situ reaction chamber. Prior to the FTIR studies, *ca.* 20 mg of the catalyst materials were finely ground and placed in the FTIR cell. The samples were activated in flowing helium gas at 673 K for 1 h and a background spectrum was taken. Then, the reactant, i.e., C_2H_4, diluted with high purity helium was introduced into the reaction chamber with a flow rate of 2 mL/min and time-resolved spectra were recorded with a resolution of 4 cm^{-1} and an accumulation of 128 scans.

The amounts of entrapped organic compounds over the catalysts after the ETP reactions performed with different time-on-stream (TOS) were analyzed by thermogravimetric analysis (TGA) on a Setram Setsys 16/18 thermogravmetric analyzer. In a typical measurement, 0.1 g of the used catalyst materials were heated in an Al_2O_3 crucible with a constant heating rate of 10 K/min and under flowing synthetic air (30 mL/min).

The nature of occluded hydrocarbons in the catalysts after the ETP reaction with different TOS was analyzed by ultraviolet–visible spectroscopy (UV–Vis) and gas chromatography–mass

spectrometry (GC–MS). The UV–Vis spectra of the fresh and used samples (ca. 100 mg) were recorded in air against $BaSO_4$ in the region of 200–800 nm on a Varian Cary 300 UV–Vis spectrophotometer. For GC–MS analysis, typically, 0.1 g of the catalyst samples obtained after the ETP reaction were carefully dissolved in 1 M HF solution. This solution was treated with CH_2Cl_2 to extract the organic compounds and the residual water was removed by the addition of sufficient sodium sulfate solid. Then, 0.2 μL of the organic extract was analyzed by GC–MS (GCMS-QP2010 SE) with a RXI-5MS column (30 m, 0.25 mm i.d., stationary phase thickness 0.25 μm). The following temperature program was employed: Isothermal heating at 313 K for 6 min, heating to 553 K with a rate of 10 K/min, and isothermal heating at 553 K for 10 min.

2.4.1. ^1H MAS NMR characterization of surface sites

The Brønsted acid sites of the fresh and used samples were characterized by means of ^1H MAS NMR spectroscopy utilizing a Bruker Avance III 400WB spectrometer at the resonance frequency of 400.1 MHz, with $\pi/2$ single pulse excitation, the repetition time of 10 s, and the sample spinning rate of 8.0 kHz using a 4.0 mm MAS NMR probe. Before the ^1H MAS NMR studies of the fresh HSSZ-13 and deAl-SSZ-13 catalysts, these materials were dehydrated at 673 K in vacuum (pressure below 10^{-2} Pa) for 10 h. Subsequently, the materials were sealed and kept in glass tubes until their transfer into gas-tight MAS NMR rotors inside a glove box purged with dry nitrogen gas. The used deAl-SSZ-13 catalysts were obtained after quenching the ETP reaction and transferring them into MAS NMR rotors without contact to air. The determination of the number of accessible Brønsted acid sites was performed upon adsorption of ammonia at room temperature and by evaluating the ^1H MAS NMR signals caused by ammonium ions (δ_{1H} = 6.5–7.0 ppm). For this purpose, the catalyst samples were loaded with 100 mbar ammonia and, subsequently, evacuated at 453 K for 2 h to eliminate physisorbed ammonia. Quantitative ^1H MAS NMR measurements were performed by comparing the signal intensities of the samples under study with the intensity of an external intensity standard (dehydrated zeolite H, Na-Y with the cation exchange degree of 35%). The decomposition and simulation of NMR spectra were carried out utilizing the Bruker software WINFIT.

3. Results and discussion

3.1. Physicochemical properties of the catalyst materials

Fig. S1 shows the powder XRD patterns of the calcined sample materials under study. Typical diffraction lines corresponding to MOR (H-Mor), BEA (H-Beta), EUO (H-EU-1), MFI (H-ZSM-5), and CHA (HSSZ-13 and SAPO-34) framework structures are observed [30], indicating that pure phases of these topologies were obtained for the microporous catalysts under study.

Due to the low base strength of acetonitrile, the adsorption of this probe molecule in the deuterated state (CD_3CN) on zeolite catalysts allows the discrimination of Brønsted acidic bridging OH groups with different acid strengths. In this case, the adsorbate-induced low-field shift $\Delta\delta_{1H}$ of the ^1H MAS NMR signal of Si(OH)Al groups is utilized as a measure of the acid strength [31–34]. A strong low-field shift $\Delta\delta_{1H}$ corresponds to a high acid strength. The interaction of acetonitrile molecules with the Brønsted acidic Si(OH)Al groups occurs *via* an O—H···N-type hydrogen bonding [33,34]. Fig. 1 shows the ^1H MAS NMR spectra of dehydrated samples recorded before and after loading with CD_3CN. Upon adsorption of acetonitrile, the signals of accessible Si(OH)Al groups (3.6–3.9 ppm) are low-field-shifted by $\Delta\delta_{1H}$ = 6.5, 6.5, 6.5, 6.8, 7.3, and 5.6 ppm for zeolites H-Mor, H-Beta, H-SSZ-13, H-EU-1, H-ZSM-5, and SAPO-34, respectively. This finding implies that Brønsted acid sites with similar strengths are present in the aluminosilicate zeolites under study, but a significantly lower acid strength was observed for the silicoaluminophosphate SAPO-34.

The adsorption of ethene on the catalysts is one of the initial steps of the ethene conversion and, thus, the adsorption behavior is a very important property of ETP catalysts. However, the adsorption of ethene on the catalysts under reaction conditions is difficult to measure, e.g. due to the fast coke formation. Therefore, low-temperature breakthrough experiments at 298 K were performed to extrapolate the adsorption of ethene on the catalyst materials. Fig. 2 shows the breakthrough curves of an ethene/helium mixture through a column filled with 0.2 g catalyst material at 298 K and 1 atm. For the blank experiment without catalyst, ethene immediately broke through the column and was monitored by mass spectrometry. In the case of catalyst-filled columns, ethene is adsorbed on the catalysts until it breaks through the column after reaching saturation. The breakthrough times in Fig. 2 hint to ethene adsorption capacities according to the sequence H-SSZ-13 (9.5 min) > SAPO-34 (7.0 min) > H-ZSM-5 (4.0 min) > H-EU-1 (2.5 min) > H-Beta (1.5 min) > H-Mor (1.0 min). This sequence indicates that the ethene adsorption properties of the catalysts under study are highly influenced by their pore structure. H-SSZ-13 and SAPO-34 with large chabazite cages, directly connected via 8-ring windows, have much higher adsorption capacities for ethene than H-ZSM-5 and H-EU-1 with medium 10-ring pores as well as H-Beta and H-Mor with large 12-ring pores.

3.2. Investigation of the ETP conversion on the zeolite catalysts under study

Table 1 gives a summary of the catalytic properties of the zeolites under study characterized by different pore structures and applied for the direct conversion of C_2H_4 at 673 K for TOS = 15 min. The propene selectivity given in column 3 strongly depends on the pore size of the various zeolite catalysts. Zeolites SAPO-34 and H-SSZ-13 consisting of large chabazite cages connected via 8-ring windows exhibit a significantly higher propene selectivity propene (>59%) and lower butene selectivity (<9%) than zeolites H-EU-1 and H-ZSM-5 with 10-ring pores as well as zeolites H-Mor and H-Beta with 12-ring pores. The latter four catalysts exhibit propene selectivities of <45% and butene selectivities of >20%. This finding may hint to a product shape-selectivity of the zeolites under study since butene with the larger kinetic diameter compared to propene can more easily desorb via the 12-ring and 10-ring pores of H-Mor, H-Beta, H-EU-1, and H-ZSM-5 than via the 8-ring windows of SAPO-34 and H-SSZ-13. In addition, the sequence of the ethene conversions over these catalysts is: H-SSZ-13 (82.9%) > SAPO-34 > (62.4%) > H-ZSM-5 (57.2%) > H-EU-1 (30.3%) > H-Beta (9.1%) > H-Mor (2.4%). These results fit well with the results of breakthrough curves (*vide supra*), indicating that the ethene adsorption abilities of the microporous catalysts strongly influence their activities in the ETP conversion. The aluminosilicate-type H-SSZ-13 catalyst with 3-dimensional structures and 8-membered rings, has the strongest ethene adsorption capacity, consequently exhibits the best activities in the ETP conversion. In order to get more insight into the ETP reaction, more detailed studies were performed on H-SSZ-13 catalyst.

3.3. Effect of dealumination of H-SSZ-13 on the catalytic performance

Dealumination of the framework by liquid acids is an important method to modify the catalytic properties of zeolites. Typically, the removal of Al from the framework results in lower density of Brønsted acid sites, but also in an enhanced acid strength. In order to investigate the effects of Brønsted acid sites on the catalytic activities of H-SSZ-13 catalysts, a homologous series of

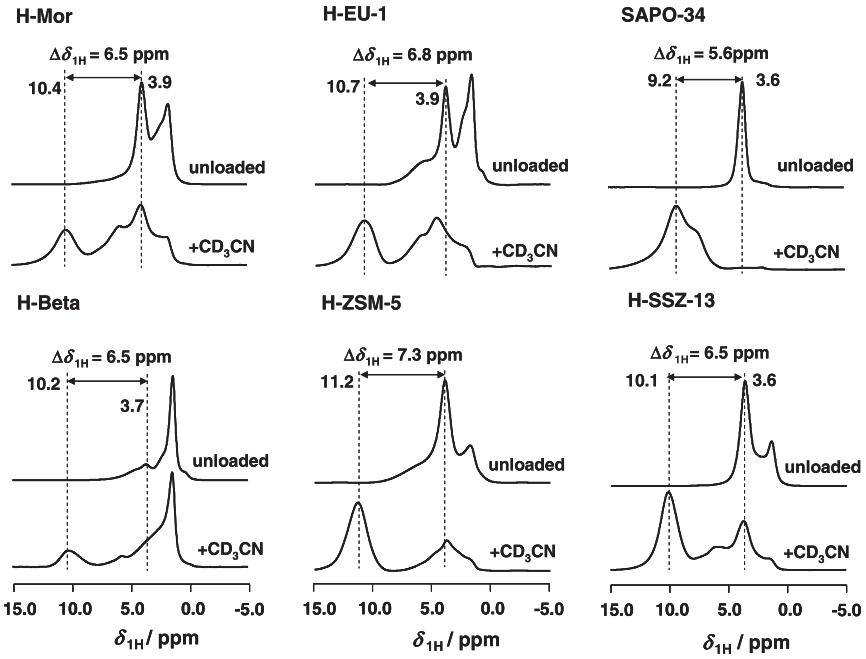

Fig. 1. ^{1}H MAS NMR spectra of dehydrated samples recorded before (bottom) and after (top) loading with deuterated acetonitrile (CD_3CN).

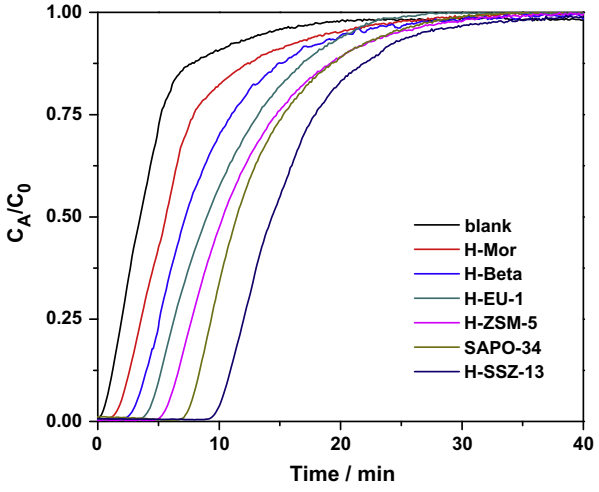

Fig. 2. Breakthrough curves of ethene of the ETP catalysts under study, recorded at 303 K.

Table 1
Ethene conversion and product selectivity during the ETP conversion on different samples[a].

Catalyst[b]	C_2H_4	Product selectivity (%)			
	Conversion (%)	C_3H_6	C_4H_8	C_1—C_3 alkane	others
H-Mor (11.2)	2.4	38.5	21.2	25.8	14.5
H-Beta (11.4)	9.1	43.4	20.8	25.7	10.1
H-EU-1 (10.3)	30.3	32.3	22.3	26.5	18.9
H-ZSM-5 (11.2)	57.2	40.1	21.5	18.3	20.1
SAPO-34 (0.1)	61.4	68.3	7.7	22.4	1.6
H-SSZ-13 (8.4)	82.9	59.5	9.8	27.9	2.8

[a] Reaction conditions: W = 0.20 g, T = 673 K, $P(C_2H_4)$ = 50.0 kPa, F = 20 cm^3 min^{-1}, Time on stream, 15 min.
[b] The numbers in parentheses denote the n_{Si}/n_{Al} ratios for aluminosilicates and the $n_{Si}/(n_{Al} + n_P + n_{Si})$ ratio for SAPO-34, determined by ICP-AES.

dealuminated sample was prepared by changing the time of acid treatment (see Section 2.1). Possible structural changes in the dealuminated H-SSZ-13 zeolites due to the dealumination procedures were investigated by X-ray diffraction (Fig. S2). The unchanged diffraction lines clearly reveal that the framework structure is well preserved after dealumination, which were further confirmed by the similar type I adsorption/desorption isotherms in nitrogen physisorption for all H-SSZ-13 samples (Fig. S3).

The textural properties of the parent and treated H-SSZ-13 zeolites are given in Table 2. After dealumination for 20 h, i.e. deAl-SSZ-13(20), the n_{Si}/n_{Al} ratio slightly increased (column 2), while the number of Brønsted acidic bridging OH groups (Fig. S4 and Table 2, column 6) and the BET surface area (column 4) decreased. However, with increasing time of acid treatment from 20 to 60 h, i.e. deAl-SSZ-13(20) to deAl-SSZ-13(60), the n_{Si}/n_{Al} ratios, numbers of Brønsted acid sites, and BET surface areas did not change, and the degree of dealumination kept stable at about 14% (Table 2, last column), which is also supported by the ^{27}Al MAS NMR spectra in Fig. S5. Both the spectra of the parent and acid-treated H-SSZ-13 zeolites are dominated by signals of tetrahedrally coordinated framework Al atoms (58.1 ppm) within the CHA framework, and only weak signals with similar intensities of few octahedrally coordinated Al species (−2.1 ppm), corresponding to extra-framework Al species, are present [35]. These results imply that the H-SSZ-13 catalyst in this study has a high resistance to dealumination by acid treatment, which agrees with an earlier report on ZSM-5 [36]. Similar to the observed framework dealumination of H-SSZ-13, the lifetime of the catalyst obviously increased after acid treatment for 20 h, but did not change obviously with the extension of the acid treatment time from 20 h to 40 and 60 h (see Fig. S6).

In Fig. 3, the time-on-stream dependence of the ethene conversion and product selectivities over the parent and dealuminated H-SSZ-13 catalysts, determined in a fixed-bed reactor at 673 K, are shown. The product distribution for deAl-SSZ-13(20) is almost similar to that of parent H-SSZ-13. Although parent H-SSZ-13 exhibited sufficient catalytic activity for the ETP conversion, it was rapidly deactivated, and the lifetime with about 50% yield of propene was 4 h. This deactivation was probably caused by the large amount of coke (25.4% weight loss after 12 h of the reaction, see Fig. S7) formed on the catalyst. In contrast, zeolite deAl-SSZ-13(20) exhibits a much longer lifetime of 7 h with about 50% yield

Table 2
Chemical composition and surface area of the calcined H-SSZ-13 and deAl-SSZ-13 materials under study.

Samples	n_{Si}/n_{Al}[a]	n_{Al}[a] (mmol/g)	S_{BET}[b] (m^2/g)	V_{micro}[c] (cm^3/g)	$n_{Si(OH)Al}$[d] (mmol/g)	$n_{Al(OH)}$[d] (mmol/g)	$n_{Si(OH)}$[d] (mmol/g)	DeAl-deg.[e] (%)
H-SSZ-13	8.4	1.58	823	0.28	1.17	0.40	0.25	-
deAl-SSZ-13(20)	9.5	1.37	774	0.26	0.96	0.36	0.27	13.3
deAl-SSZ-13(40)	9.4	1.36	764	0.25	0.99	0.35	0.28	13.9
deAl-SSZ-13(60)	9.5	1.36	746	0.24	0.97	0.38	0.35	13.9

[a] Determined by ICP-AES.
[b] Determined by N_2-absorption.
[c] Micropore volume was estimated by using the *t*-plot method.
[d] Determined by ^{1}H MAS NMR.
[e] Calculated by the concentrations of Aluminum (column 3).

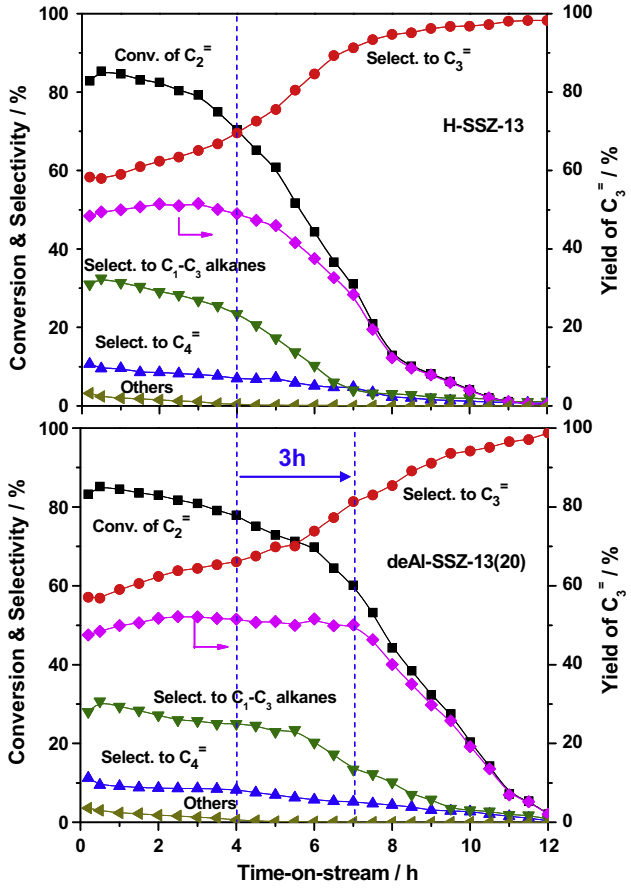

Fig. 3. Ethene conversion over H-SSZ-13 and deAl-SSZ-13(20) sample (W = 0.20 g, T = 673 K, $p(C_2H_4)$ = 50.0 kPa, F = 20 mL/min, TOS = 12 h).

of propene during the ETP conversion, and it also showed a significantly lower coke formation (19.3% weight loss after 12 h of the reaction, see Fig. S7). This lower tendency for coke formation is probably caused by the decreased number of Brønsted acid sites, indicating that dealuminated H-SSZ-13 is the better ETP catalyst with prolonged life-time.

3.4. Effects of reaction conditions of the ETP conversion on the deAl-SSZ-13(20) zeolite

Fig. 4 shows the ethene conversion and product distribution over deAl-SSZ-13(20) at reaction temperatures of 573–723 K. Clearly, ethene conversion gradually increases with increasing reaction temperature up to 673 K, and it starts to decrease for 723 K. Simultaneously, the selectivity to propene gradually increases, while the selectivities to larger products decrease. This

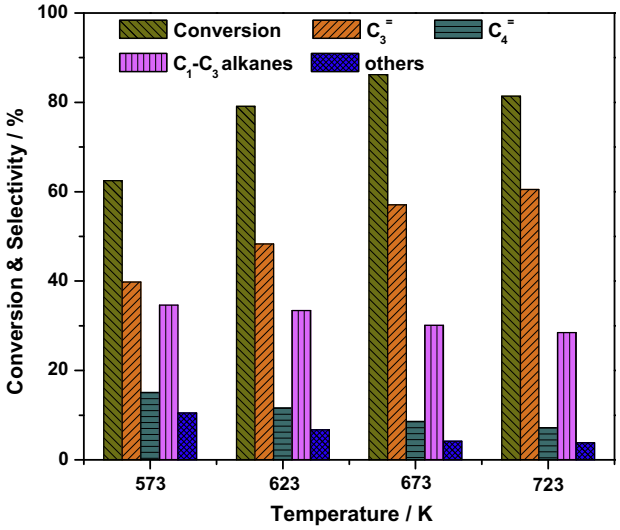

Fig. 4. Ethene conversion and product distribution over deAl-SSZ-13(20) at different temperatures (W = 0.20 g, $p(C_2H_4)$ = 50.0 kPa, F = 20 mL/min, TOS = 1 h).

finding can be explained by an increasing tendency toward cracking of heavier hydrocarbons to lighter fragments, i.e. ethene and propene, with increasing reaction temperatures.

Fig. 5 shows the change in the ethene conversion and product distribution as a function of the weight of deAl-SSZ-13(20) applied in the ETP conversion, which corresponds to a modification of the contact time. Obviously, the longer contact time in the case of the higher catalysts weight results in a higher ethene conversion, but lower propene selectivity. Simultaneously, the selectivity to C_1—C_3 alkanes strongly increases. This may be a hint that hydrogen transfer reactions more easily occur if the main product propene has longer contact time with active Brønsted acid sites on the deAl-SSZ-13 catalyst. Consequently, the higher selectivity to C_1—C_3 alkanes is expected and also obtained for reaction systems with higher weight of catalyst.

Under optimum reaction conditions (*vide supra*), i.e. 0.2 g deAl-SSZ-13(20) and a reaction temperature of 673 K, the possibility of regeneration of used deAl-SSZ-13(20) catalysts was investigated by calcination in synthetic air at 873 K for 4 h. The ethene conversions and product selectivities in Fig. 6 show that the catalytic performance could be well recovered for the regenerated catalysts. After two reaction/regeneration cycles (Fig. 6, right), the catalytic performance is the same as that of the fresh material (Fig. 6, left). This indicates that carbon deposits are mainly responsible for the deactivation of the deAl-SSZ-13(20) catalysts.

In order to get detailed information on the reaction mechanism and the deactivation behavior of the deAl-SSZ-13 catalyst during the ETP reaction, the nature of the organic deposits responsible for the catalyst deactivation and the fate of active surface species

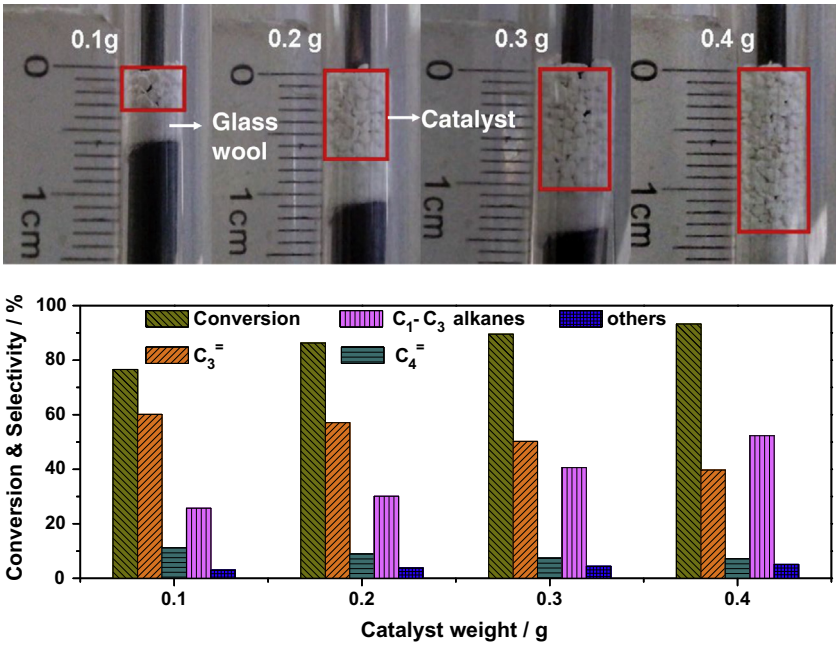

Fig. 5. Ethene conversion and product distribution over deAl-SSZ-13(20) with different mass weight at 673 K (W = 0.1–0.40 g, $p(C_2H_4)$ = 50.0 kPa, F = 20 mL/min, TOS = 1 h).

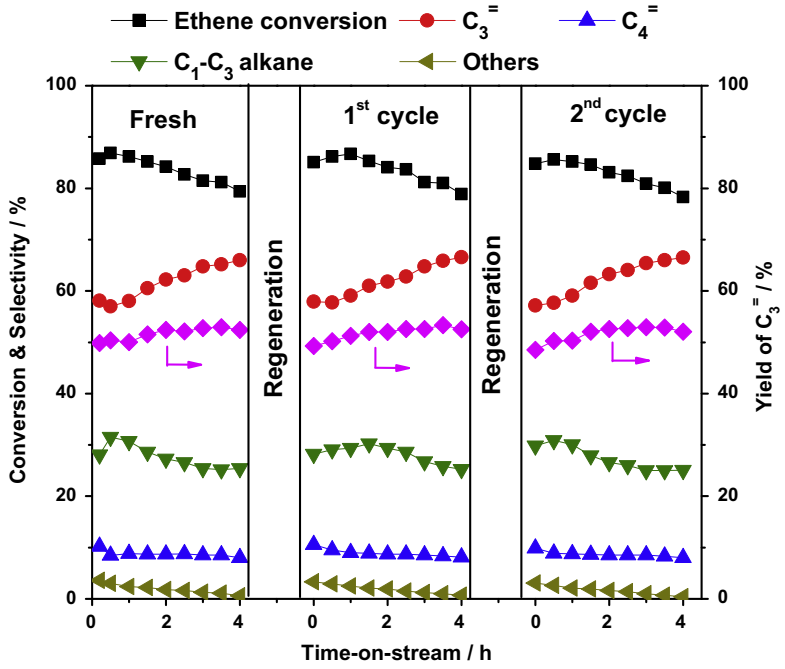

Fig. 6. Catalytic properties of generated deAl-H-SSZ-13(20) zeolites used as ETP catalysts at 673 K (W = 0.20 g, $p(C_2H_4)$ = 50.0 kPa, F = 20 mL/min, TOS = 4 h).

during the catalyst lifetime were investigated via in situ FTIR, ex situ UV/Vis, TGA, GC–MS, and ^{1}H MAS NMR spectroscopy in further studies.

3.5. In situ FTIR studies of the ETP reaction on deAl-SSZ-13(20)

The in situ FTIR spectra of the species adsorbed and occluded on deAl-SSZ-13(20) under ETP reaction conditions at 673 K are shown in Fig. 7 A. The appearance of negative bands at 3605 cm^{-1} after starting the ethene flow indicates that reactants, such as ethene or reaction products, gradually cover Brønsted acidic bridging OH groups (Si(OH)Al) [37]. Simultaneously, the appearance of weak negative bands of terminal silanol groups at 3740 cm^{-1} and a negative shoulder at 3705 cm^{-1} can be observed, indicating interactions between ethene and various types of silanol groups, in accordance with the earlier studies of Wang et al. [24]. Positive bands at 1424, 1485 and 3000–3120 cm^{-1} are attributed to C—H bending vibrations and C—H stretching vibrations of weakly adsorbed ethene, while bands at 1385 and 1460 cm^{-1} are due to C—H bending vibrations of CH_2 and CH_3 groups, respectively, of reaction products [34]. The latter bands indicate that oligomerization of ethene occurs immediately after starting the ETP conversion [38]. Subsequently, new bands at 1605, 1570, 1502 cm^{-1}, and 2860–2930 cm^{-1} appear, which can be explained by skeletal C=C

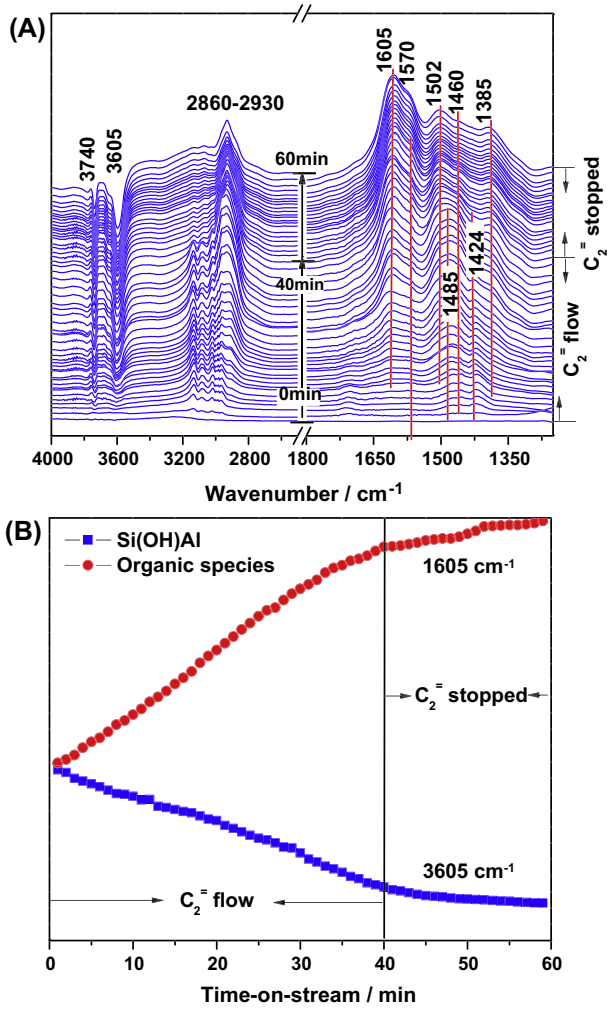

Fig. 7. In situ FTIR spectra recorded during ethene conversion over deAl-SSZ-13(20) at 673 K up to TOS = 1 h (A) and intensity of the Si(OH)Al band at 3605 cm^{-1} and the band of organic deposits at 1605 cm^{-1} recorded during ethene conversion over deAl-SSZ-13(20) at 673 K up to TOS = 1 h (B).

vibrations of aromatics and C—H stretching vibrations, respectively [39–41]. These bands hint to a rapid formation of aromatics during the ETP conversion on deAl-SSZ-13(20).

After stopping the ethene flow and starting the purging with helium, the bands at 1424–1485 and 3000–3120 cm^{-1} due to the weakly adsorbed ethene disappeared, while the bands at 1605, 1570, 1502, 1460, and 1385 cm^{-1} still remain and keep stable. Hence, the organic deposits formed during the ETP reaction are very stable. The intensities of the bands of Brønsted acidic Si(OH)Al groups at 3605 cm^{-1} and of aromatic species formed during the ETP conversion at 1605 cm^{-1} are shown in Fig. 7 B. Clearly, the Brønsted acid sites are gradually covered by ethene or reaction products upon starting the ethene flow at reaction temperature, while aromatic species are gradually formed simultaneously. After stopping the ETP reaction by stopping the ethene flow, the coverage of Brønsted acid sites and the number of aromatic species gradually keep stable.

3.6. TGA, UV/Vis, and GC–MS analysis of organic deposits on the used deAl-SSZ-13(20) catalysts

For quantifying the organic deposits formed on deAl-SSZ-13(20) after the ETP conversion for TOS = 0.25–12 h, the weight loss was determined by TGA in the temperature range of 293 to 1073 K. In general, two obvious weight losses can be recognized: A low-temperature weight loss, Δw_{lt}, at <573 K and a high-temperature weight loss, Δw_{ht}, at >673 K, which are ascribed to desorption of volatile compounds and occluded coke compounds, respectively. According to Fig. 8, the deAl-SSZ-13(20) samples obtained after TOS = 0.25 h, 0.5 h, and 1.0 h show a similar low-temperature weight loss Δw_{lt} of about ca. 5%, while the samples obtained after TOS = 2.0 h, 4.0 h, 8.0 h, and 12 h are characterized by a significantly lower weight loss Δw_{lt} of ca. 3% in this temperature range. This finding indicates that much more volatile organic compounds are formed up to TOS = 1 h compared to TOS $\geqslant$ 2.0 h. In the high-temperature range of 573 to 1073 K, the weight losses are increased from 2.8% to 19.8% with the progress of the ETP conversion from TOS = 0.25 h to 12 h, indicating the organic compounds are gradually accumulated on the deAl-SSZ-13(20) catalyst. In addition, the high-temperature weight loss Δw_{ht} of the deactivated deAl-SSZ-13(20) catalyst obtained after TOS = 12 h is only 0.6% larger than the Δw_{ht} value of the active sample obtained after TOS = 8 h. This finding indicates that only few coke deposits are required to cause a significant deactivation of deAl-SSZ-13(20) in the ETP conversion.

The nature of organic deposits formed on deAl-SSZ-13(20) during the ETP conversion and after TOS = 0.25–12 h was investigated by ex situ UV/Vis spectroscopy. According to Fig. 9, UV/Vis bands at 220, 276, and 400 nm occur during the initial 0.25 h. With the further progress of reaction, the bands at 220 and 276 nm shift to 233 and 288 nm, and additional bands occur at 445–475 nm. Based on earlier UV/Vis studies of organic compounds on acidic zeolite catalysts [42–49], the band at 220 nm is assigned to UV/Vis sensitive dienes, while the bands at ca. 276 nm may be due to aromatic species or monoenylic carbenium ions [46]. The red shift of these bands to 233 and 288 nm, respectively, for increasing TOS could indicate that carbon chain growth or cyclization reactions occur [47]. Bands at 350–420 nm hint to the formation of dienylic carbenium ions and polycyclic aromatics [45,46,48]. The latter species formed with two or three condensed aromatic rings occur at wavelengths lower than 400 nm, while those formed with four condensed aromatic rings occur at wavelengths slightly higher than 400 nm [49]. Broad bands occurring at 445–475 nm may be caused by trienylic carbenium ions [47]. The concentrations of all organic species, reflected as the intensities of corresponding UV/Vis bands, change strongly with the progress of the ETP reaction. Upon TOS = 1.0 h, the amount of dienes (220–233 nm) decreases, which fits well with the performance of the low-temperature weight loss Δw_{lt} during the TGA studies (Fig. 8, left). Simultaneously, the

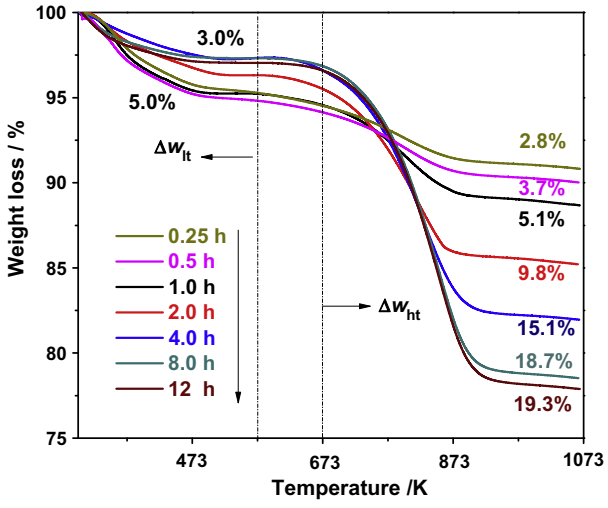

Fig. 8. TGA curves of used deAl-SSZ-13 catalysts obtained after different TOS.

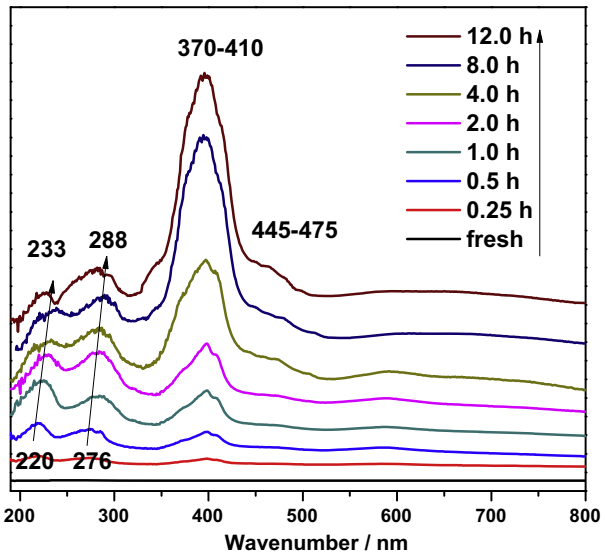

Fig. 9. Ex situ UV/Vis spectra of deAl-SSZ-13 catalysts obtained after different TOS.

amounts of aromatic species (276–288 nm) and polycyclic aromatics (370–410 nm) increase with increasing TOS, which also agrees very well with the high-temperature weight loss Δw_{ht} (Fig. 8, right).

The chemical composition of the organic deposits occluded in the used deAl-SSZ-13(20) samples was analyzed by ex situ GC–MS and the results are shown in Fig. 10. Mainly, organic species consisting of two or three aromatic rings, such as alkylnaphthalenes and anthracene were detected. Typically, polymethyl-isopropylnaphthalenes are observed as major organic species occluded in the used catalyst samples obtained up to TOS = 4 h. According to Fig. 10, the amounts of polymethyl-isopropylnaphthalenes (isopropylnaphthalenes, monomethyl-isopropylnaphthalenes, and dimethyl-isopropylnaphthalenes) increase with increasing TOS and reach a maximum at TOS = 4.0 h. Simultaneously, the deAl-SSZ-13(20) catalyst exhibits a good activity in the ETP reaction (Fig. 3). After TOS = 8.0 h, the number of polymethyl-isopropylnaphthalenes strongly decreases, while naphthalenes, 1-methylnaphthalenes, and anthracene become the dominating organic compounds. At the same time, a deactivation of the deAl-SSZ-13 catalyst occurs, and the total deactivation can be observed at TOS = 12 h. This may indicate that polymethyl-isopropylnaphthalenes are the most active organic species in the ETP conversion, from which propene can be split. Once the catalyst starts the deactivation (TOS = 8.0 h), large coke compounds, e.g. anthracene, are rapidly formed and block the cages and 8-ring windows of deAl-SSZ-13(20), also the Brønsted acid sites, and no more polymethyl-isopropylnaphthalenes can be formed near the Brønsted acid sites, resulting in the total deactivation of the catalyst.

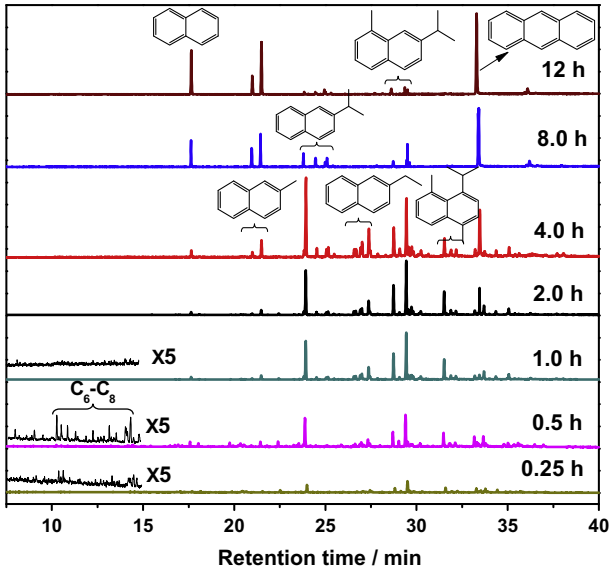

Fig. 10. GC–MS chromatograms of the extracts from used deAl-SSZ-13(20) catalysts obtained after different TOS.

3.7. ^{1}H MAS NMR studies of the fate of Brønsted acid sites and carbenium species during the ETP reaction

In order to investigate the fate of Brønsted acid sites and carbenium-type organic species on deAl-SSZ-13 samples, the calcined (TOS = 0 h) and used deAl-SSZ-13(20) samples obtained after TOS = 0.5–12 h were investigated by ^{1}H MAS NMR spectroscopy with and without ammonia loading (Fig. 11, left and right, respectively). The ^{1}H MAS NMR spectrum of the calcined (TOS = 0 h) deAl-SSZ-13(20) (Fig. 11, top, left) is dominated by a signal at 3.7 ppm caused by Brønsted acidic Si(OH)Al groups. Adsorption of ammonia on accessible Brønsted acid site leads to the formation of ammonium ions with a ^{1}H MAS NMR signal at 6.1 ppm (Fig. 11, top, right). After TOS = 0.5 h, strong signals at 1.7–2.2 ppm and 7.4–9.7 ppm corresponding to hydrogen atoms bound to aliphatic and aromatic carbon atoms [44], respectively, can be observed in the ^{1}H MAS NMR spectrum. Meanwhile, the intensity of the signal at 3.7 ppm due to Brønsted acid site in deAl-SSZ-13(20) decreases significantly. After ammonia loading at room temperature, a new signal caused by the reaction of ammonia with organic deposits occurs at 4.7 ppm. In a former study of the MTO conversion over SAPO-34 zeolite, a signal at 5.1 ppm was explained by the formation of polyalkylphenylammonium ions by the reaction of ammonia with polyalkylbenzenium ions [44]. According to the results of in situ UV/Vis spectroscopy and GC/MS analysis of organic deposits (Section 3.5), the aromatic-type carbenium ions formed during the ETP reaction over deAl-SSZ-13(20) catalyst are probably polyalkylnaphthalene-based carbenium ions. Upon adsorption of ammonia, formation of amines occurs at these carbenium species leading to a new signal at 4.7 ppm due to NH_2 groups [50]. Caused by the much stronger steric constrains of polyalkylnaphthalenes compared to polyalkylbenzenes in the chabazite cages of HSSZ-13 and SAPO-34, ammoniated polyalkylnaphthalenes cannot be stabilized as carbenium ions, but form amines in the used and ammonia-loaded deAl-SSZ-13(20) catalysts.

In Fig. 12, the number of accessible bridging OH groups, n_{SiOHAl}, and the number of polyalkylnaphthalene-based carbenium ions, $n_{carbenium}$, which react with ammonia to a corresponding amine, both determined by quantitative ^{1}H MAS NMR spectroscopy, are plotted as a function of TOS. The number of accessible Si(OH)Al groups strongly decreases from 0.96 mmol/g for TOS = 0 h to 0.40 mmol/g after TOS = 0.5 h. At the same time (TOS = 0.5 h), 0.45 mmol/g naphthalene-based carbenium ions are formed. After TOS = 2.0 h, the number of naphthalene-based ions increases to 0.69 mmol/g, while the number of Brønsted acid sites decreases to 0.14 mmol/g. With the further progress of the reaction, the number of naphthalene-based ions starts to decrease and decreases to 0.46 mmol/g after TOS = 8.0 h, while the number of accessible Brønsted acid sites reaches nearly a value of 0 mmol/g. Interestingly, the deAl-SSZ-13(20) catalyst still exhibited an ETP activity according to an ethene conversion of 40% at TOS = 8.0 h. After deactivation of deAl-SSZ-13(20) at TOS = 12 h, neither accessible Brønsted acid sites nor naphthalene-based carbenium ions can be detected by ^{1}H MAS NMR spectroscopy. This observation indicates

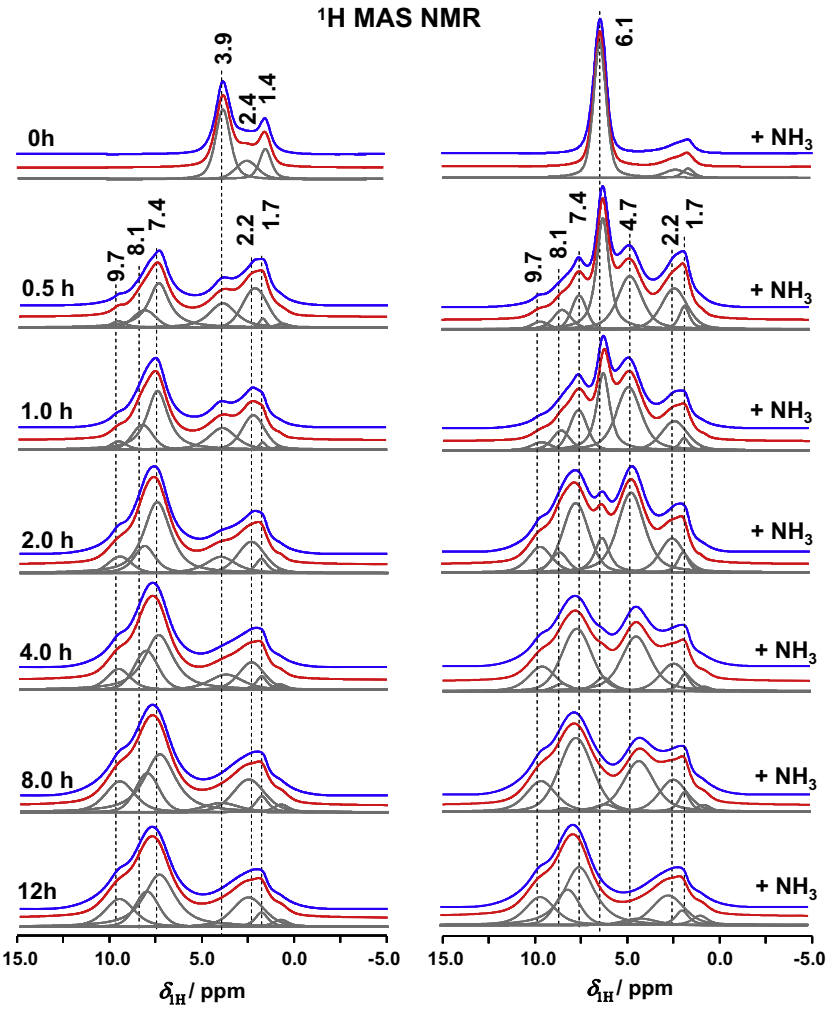

Fig. 11. ^{1}H MAS NMR spectra of used deAl-SSZ-13(20) catalysts obtained after different TOS and recorded before (left) and after (right) adsorption of ammonia. From top to bottom, the experimental spectra, the simulated spectra, and the signal components utilized for the simulation are shown.

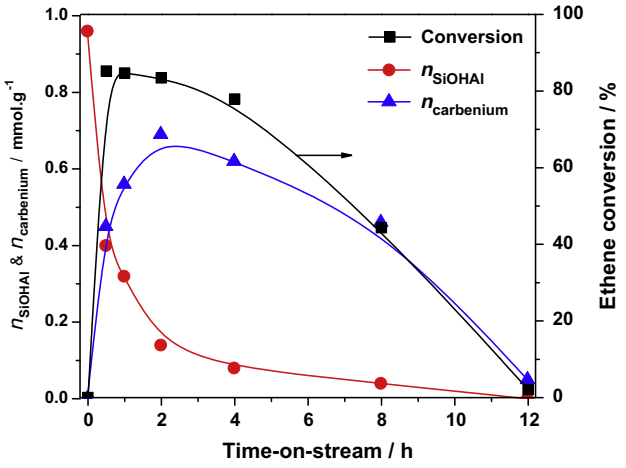

Fig. 12. Comparison of the ethene conversion and the numbers of Si(OH)Al groups (n_{SiOHAl}) and carbenium ions ($n_{carbenium}$), determined by quantitative ^{1}H MAS NMR spectroscopy.

that naphthalene-based carbenium ions play a key role as catalytically active organic compounds during the ETP conversion over deAl-SSZ-13(20). Therefore, the total consumption of the accessible Brønsted acid sites and naphthalene-based carbenium ions leads to a complete deactivation of the deAl-SSZ-13(20) catalyst.

3.8. Reaction mechanism of ETP reaction over SSZ-13

In the present work, a number of complementary methods, such as TGA, GC–MS, in situ FTIR, ex situ UV/Vis, and ^{1}H MAS NMR spectroscopy, gave insights into different aspects of the ethene-to-propene conversion on dealuminated H-SSZ-13 zeolites including the deactivation of this catalyst during the ETP reaction.

As demonstrated by in situ FTIR spectroscopy, ethene is rapidly oligomerized and converted to aromatics after starting the conversion at 673 K. With the progress of the ETP conversion, the aromatics are gradually accumulated, and large aromatics with two to three condensed aromatic rings are rapidly formed, which can be supported by UV/Vis and GC–MS measurements. Naphthalene-based carbenium ions, evidenced by quantitative ^{1}H MAS NMR spectroscopy, play the active reaction intermediates in ETP conversion, to which ethene is added and from which propene are split in a closed cycle (Scheme 1), similar to the hydrocarbon pool mechanism in the MTO reaction [51–55]. Hence, in contrast to SAPO-34 forming hexylcarbenium ions and/or the 4-methyl-2-pentylcarbenium ions during the induction period of the ETP reaction [23], these organic species were not observed during the ETP conversion on H-SSZ-13 catalyst. This finding indicates that hexylcarbenium

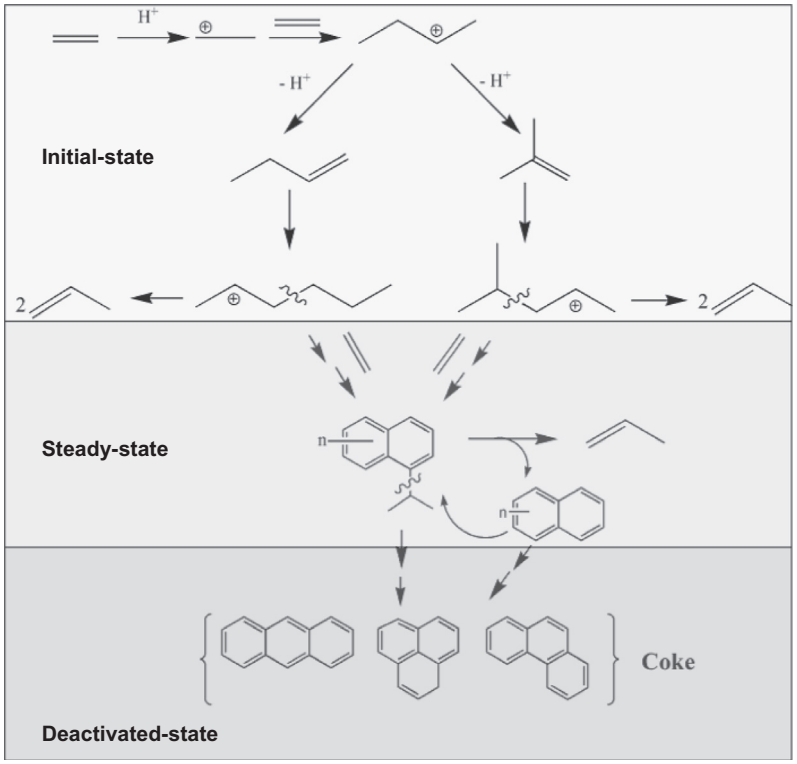

Scheme 1. Reaction scheme.

ions and/or the 4-methyl-2-pentylcarbenium ions are rapidly converted to larger naphthalene-based carbenium ions on H-SSZ-13. Since these different catalytic properties of SAPO-34 and HSSZ-13 in the ETP reaction cannot be caused by different steric constrains (both CHA-type zeolites), the above-mentioned different catalytic properties may be due to the different strengths of their Brønsted acid sites. This difference in the acid strength of zeolites SAPO-34 and HSSZ-13 was clearly evidenced by ^{1}H MAS NMR spectroscopy of the acetonitrile loaded materials (see Section 3.1 and Fig. 1).

Considering the Brønsted acidity as a key property of the H-SSZ-13 catalyst for its application in the heterogeneously catalyzed ETP reaction, ^{1}H MAS NMR spectroscopy was applied to investigate the fate of Brønsted acid sites during ETP conversion process. The number of accessible Brønsted acid sites of deAl-SSZ-13 strongly decreased already after a short reaction time of 0.5 h. Interestingly, already before the total deactivation of the deAl-SSZ-13 catalysts under study occurred, nearly no accessible Brønsted acid sites could be detected by ^{1}H MAS NMR spectroscopy. On the other hand, while the number of accessible Brønsted acid sites decreased, the number of naphthalene-based carbenium ions increased during the highly active reaction period of the deAl-SSZ-13 catalyst. The above-mentioned observation indicates that naphthalene-based carbenium ions play a key role as catalytically active intermediates in the ETP conversion over H-SSZ-13. This statement is supported by the absence of accessible naphthalene-type carbenium species in the totally deactivated deAl-SSZ-13 catalyst.

In addition, because of the high reactivity of the carbenium species, a surplus of these species in the SSZ-13 cages and pores is accompanied with their rapid transformation, such as the formation of polycyclic aromatics as indicated by UV/Vis spectroscopy (UV/Vis bands at ca. 400 nm). Finally, these polycyclic aromatics cause a total blocking of the SSZ-13 pores, which strongly hinders the diffusion of reaction products and make all catalytically active sites and species non-accessible for further reactants, which was demonstrated in our recently published PFG NMR study on ethene diffusion in SAPO-34 used as MTO catalysts [43]. Compared with the parent H-SSZ-13 zeolite, the dealuminated H-SSZ-13 (deA-SSZ-13(20)) catalyst are characterized by a much slower coke formation due to its lower Brønsted acid site density, making this material an interesting catalyst with prolonged lifetime in the ETP conversion.

4. Conclusions

In the present work, several types of microporous molecular sieves with different pore structures were studied as ETP catalysts. The aluminosilicate H-SSZ-13 catalyst with chabazite cages directly connected via 8-ring windows and the strongest adsorption capacity for ethene exhibits the best activity in the ETP conversion. After dealumination of the parent H-SSZ-13 zeolite, prolonged lifetime could be obtained over deAl-SSZ-13 applied as catalyst in the ETP conversion, since the velocity of coke formation was reduced via decreasing the Brønsted acid site densities.

For elucidating the reaction mechanism and the deactivation behavior of the deAl-SSZ-13 catalyst, in situ FT-IR, ex situ UV/Vis spectroscopy, and GC–MS were employed to monitor the formation and nature of organic deposits during the ETP conversion. The amounts of organic deposits formed during the ETP process were determined by TGA. The nature and density of accessible Brønsted acid sites and active organic species were investigated as a function of the TOS by ^{1}H MAS NMR spectroscopy. The reaction mechanism and the deactivation behavior of the deAlH-SSZ-13(20) catalyst investigated by the above-mentioned methods can be described as follows:

(i) After starting the ethene conversion, a rapid oligomerization occurs (FTIR) leading to the formation of dienes, aromatics, and polycyclic aromatics (UV/Vis).

(ii) Polyalkylnaphthalenes as the major detected organic species play a key role in the active period of the catalyst, while these species strongly decrease upon the catalysts deactivation (GC–MS).
(iii) Already in the active period of the catalyst, a rapid and strong decrease in the density of accessible Brønsted acid sites occurs, while the number of naphthalene-based carbenium ions increases (^{1}H MAS NMR).
(iv) Caused by the accumulation of large polycyclic aromatics (UV/Vis, GC–MS), a blocking of the catalysts pores occurs. Consequently, neither Brønsted acid sites nor catalytically active carbenium ions are accessible for further reactants (^{1}H MAS NMR). This leads to a strong deactivation of the deAlH-SSZ-13 material.

Acknowledgments

This work was supported by the National Natural Science Foundation of China (21303089), China Postdoctoral Science Foundation, 111 Project (B12015), the Collaborative Innovation Center of Chemical Science and Engineering (Tianjin) and the Ministry of Education of China (NCET-11-0251, IRT13022). Furthermore, M.H. wants to thank for financial support by Deutsche Forschungsgemeinschaft.

Appendix A. Supplementary data

Supplementary data associated with this article can be found, in the online version, at http://dx.doi.org/10.1016/j.jcat.2014.03.006.

References

[1] H.-J. Arpe, Industrial Organic Chemistry, fourth ed., Wiley-VCH Verlag BmbH & Co., Weinheim, Germany, 2003.
[2] G. Ertl, H. Knözinger, F. Schüth, J. Weitkamp (Eds.), Handbook of Heterogeneous Catalysis, Wiley-VCH Verlag GmbH & Co. KgaA, Weinheim, 2008.
[3] J. Lu, Z. Zhao, C. Xu, A. Duan, P. Zhang, Catal. Lett. 109 (2006) 65.
[4] L.F. Lin, C.F. Qiu, Z.X. Zhuo, D.W. Zhang, S.F. Zhao, H.H. Wu, Y.M. Liu, M.Y. He, J. Catal. 309 (2014) 136.
[5] R.L. Banks, S.G. Kukes, J. Mol. Catal. 28 (1985) 117.
[6] J.C. Mol, J. Mol. Catal. A 213 (2004) 39.
[7] M. Conte, B. Xu, T.E. Davies, J.K. Bartley, A.F. Carley, S.H. Taylor, K. Khalid, G.J. Hutchings, Micropor. Mesopor. Mater. 164 (2012) 207.
[8] F.L. Bleken, S. Chavan, U. Olsbye, M. Boltz, F. Ocampo, B. Louis, F. Ocampo, B. Louis, Appl. Catal. A 447 (2012) 178.
[9] S. Sugiyama, Y. Kato, T. Wada, S. Ogawa, K. Nakagawa, K. Sotowa, Top. Catal. 53 (2010) 550.
[10] M. Iwamoto, K. Kasai, T. Haishi, ChemSusChem 4 (2011) 1055.
[11] P.P. O'Neill, J.J. Rooney, J. Am. Chem. Soc. 94 (1972) 4383.
[12] T. Yamaguchi, Y. Tanaka, K. Tanabe, J. Catal. 65 (1980) 442.
[13] M. Iwamoto, Y. Kosugi, J. Phys. Chem. C 111 (2007) 13.
[14] K. Ikeda, Y. Kawamura, T. Yamamoto, M. Iwamoto, Catal. Commun. 9 (2008) 106.
[15] M. Iwamoto, Catal. Surv. Asia 12 (2008) 28.
[16] M. Iwamoto, Molecules 16 (2011) 7844.
[17] L.A. Perea, T. Wolff, P. Veit, L. Hilfert, F.T. Edelmann, C. Hamel, A. Seidel-Morgenstern, J. Catal. 305 (2013) 154.
[18] A.S. Frey, O. Hinrichsen, Micropor. Mesopor. Mater. 164 (2012) 164.
[19] M. Taouk, E. LeRoux, J. Thivolle-Cazat, J.-M. Basset, Angew. Chem. Int. Ed. 46 (2007) 7202.
[20] H. Oikawa, Y. Shibata, K. Inazu, Y. Iwase, K. Murai, S. Hyodo, G. Kobayashi, T. Baba, Appl. Catal. A 312 (2006) 181.
[21] Y. Iwase, K. Motokura, T. Koyama, A. Miyaji, T. Baba, Phys. Chem. Chem. Phys. 11 (2009) 9268.
[22] T.-R. Koyama, Y. Hayashi, H. Horie, S. Kawauchi, A. Matsumoto, Y. Iwase, Y. Sakamoto, A. Miyaji, K. Motokura, T. Baba, Phys. Chem. Chem. Phys. 12 (2010) 2541.
[23] Y. Iwase, Y. Sakamoto, A. Shiga, A. Miyaji, K. Motokura, T-R. Koyama, T. Baba, J. Phys. Chem. C 116 (2012) 5182.
[24] B.M. Liu, Q.H. Zhang, Y. Wang, Ind. Eng. Chem. Res. 48 (2009) 10788.
[25] T. Lehmann, T. Wolff, V.M. Zahn, P. Veit, C. Hamel, A. Seidel-Morgenstern, Catal. Commun. 12 (2011) 368.
[26] T. Lehmann, T. Wolff, C. Hamel, P. Veit, B. Garke, A. Seidel-Morgenstern, Micropor. Mesopor. Mater. 151 (2012) 113.
[27] M. Tanaka, A. Itadani, Y. Kuroda, M. Iwamoto, J. Phys. Chem. C 116 (2012) 5664.
[28] N. Nishiyama, M. Kawaguchi, Y. Hirota, D.V. Vu, Y. Egashira, K. Ueyama, Appl. Catal. A 362 (2009) 193.
[29] W.L. Dai, G.J. Wu, L.D. Li, N.J. Guan, M. Hunger, ACS Catal. 3 (2013) 588.
[30] M.M.J. Treacy, J.B. Higgins (Eds.), Collection of Simulated XRD Powder Patterns for Zeolites, fifth revised ed., Elsevier, Amsterdam, 2007.
[31] J.F. Haw, M.B. Hall, A.E. Alvarado-Swaisgood, E.J. Munson, Z. Lin, L.W. Beck, T. Howard, J. Am. Chem. Soc. 116 (1994) 7308.
[32] J. Jaenchen, J.H.M.C. van Wolput, L.J.M. van de Ven, J.W. de Haan, R.A. van Santen, Catal. Lett. 39 (1996) 147.
[33] A. Simperler, R.G. Bell, M.W. Anderson, J. Phys. Chem. B 108 (2004) 7142.
[34] A. Simperler, R.G. Bell, M.D. Foster, A.E. Gray, D.W. Lewis, M.W. Anderson, J. Phys. Chem. B 108 (2004) 7152.
[35] S. Inagaki, S. Shinoda, Y. Kaneko, K. Takechi, R. Komatsu, Y. Tsuboi, H. Yamazaki, J.N. Kondo, Y. Kubota, ACS Catal. 3 (2013) 74.
[36] P.J. Kooyman, P. vanderWaal, H. vanBekkum, Zeolites 18 (1997) 50.
[37] G. Spoto, S. Bordiga, G. Ricchiardi, D. Scarano, A. Zecchina, E. Borello, J. Chem. Soc., Faraday Trans. 90 (1994) 2827.
[38] S. Bodoardo, R. Chiappetta, F. Fajula, E. Garrone, Micropor. Mater. 3 (1995) 613.
[39] M. Hunger, Micropor. Mesopor. Mater. 82 (2005) 241.
[40] L.M. Petkovic, D.M. Ginosar, K.C. Burch, J. Catal. 234 (2005) 328.
[41] M. Bjørgen, F. Bonino, B. Arstad, S. Kolboe, K.-P. Lillerud, A. Zecchina, S. Bordiga, ChemPhysChem 6 (2005) 232.
[42] W.L. Dai, X. Wang, G.J. Wu, N.J. Guan, M. Hunger, L.D. Li, ACS Catal. 1 (2011) 292.
[43] W.L. Dai, M. Scheibe, L.D. Li, N.J. Guan, M. Hunger, J. Phys. Chem. C 116 (2012) 2469.
[44] W.L. Dai, M. Scheibe, N.J. Guan, L.D. Li, M. Hunger, ChemCatChem 3 (2011) 1130.
[45] Y. Jiang, J. Huang, V.R. Reddy Marthala, Y.S. Ooi, J. Weitkamp, M. Hunger, Micropor. Mesopor. Mater. 105 (2007) 132.
[46] H.G. Karge, M. Laniecki, M. Ziolek, G. Onyestyak, A. Kiss, P. Kleinschmit, M. Siray, in: P.A. Jacobs, R.A. van Santen (Eds.), Zeolites: Facts, Fig.s, Future, Stud. Surf. Sci. Catal, vol. 49, Elsevier, Amsterdam, 1989, p. 1327.
[47] I. Kiricsi, H. Förster, G. Tasi, J.B. Nagy, Chem. Rev. 99 (1999) 2085.
[48] J. Mohan, Organic Spectroscopy Principles and Applications, Alpha Science International Ltd., Harrow, 2002. p. 128.
[49] J.W. Park, J.Y. Lee, K.S. Kim, S.B. Hong, G. Seo, Appl. Catal. A 339 (2008) 36.
[50] HNMR Predictor, Product Version 9.08, Advanced Chemistry Development Inc., 2006.
[51] I.M. Dahl, S. Kolboe, Catal. Lett. 20 (1993) 329.
[52] I.M. Dahl, S. Kolboe, J. Catal. 149 (1994) 304.
[53] I.M. Dahl, S. Kolboe, J. Catal. 161 (1996) 458.
[54] M. Stöcker, Micropor. Mesopor. Mater. 29 (1999) 3.
[55] M. Stöcker, in: J. Čejka, A. Corma, S. Zones (Eds.), Zeolite and Catalysis: Synthesis, Reactions and Applications, Wiley-VCH, Weinheim, 2010, p. 687.